Strain-induced phonon shifts in tungsten disulfide nanoplatelets and nanotubes

2017 2D Mater. 4 015007

(http://iopscience.iop.org/2053-1583/4/1/015007)

2D Materials

PAPER

Strain-induced phonon shifts in tungsten disulfide nanoplatelets and nanotubes

Fang Wang[1], Ian A Kinloch[1], Daniel Wolverson[2], Reshef Tenne[3], Alla Zak[4], Eoghan O'Connell[5], Ursel Bangert[5] and Robert J Young[1]

[1] School of Materials and National Graphene Institute, University of Manchester, Oxford Road, Manchester M13 9PL, UK
[2] Department of Physics, University of Bath, Claverton Down, Bath, BA2 7AY, UK
[3] Department of Materials and Interfaces, Weizmann Institute of Science, Rehovot 76100, Israel
[4] Faculty of Sciences, Holon Institute of Technology, Holon 5810201, Israel
[5] Bernal Institute, Department of Physics and Energy, University of Limerick, Limerick, Ireland

E-mail: robert.young@manchester.ac.uk

Keywords: nanotubes, deformation, Raman spectroscopy, photoluminescence, transmission electron microscopy, density functional theory, tungsten disulfide

Supplementary material for this article is available online

OPEN ACCESS

RECEIVED
10 August 2016

REVISED
6 October 2016

ACCEPTED FOR PUBLICATION
14 October 2016

PUBLISHED
28 October 2016

Abstract

The relationship between structure and properties has been followed for different nanoscale forms of tungsten disulfide (2H-WS_2) namely exfoliated monolayer and few-layer nanoplatelets, and nanotubes. The similarities and differences between these nanostructured materials have been examined using a combination of optical microscopy, scanning and high-resolution transmission electron microscopy and atomic force microscopy. Photoluminescence and Raman spectroscopy have also been used to distinguish between monolayer and few-layer material. Strain induced phonon shifts have been followed from the changes in the positions of the A_{1g} and $E_{2g}{}^1$ Raman bands during uniaxial deformation. This has been modelled for monolayer using density functional theory with excellent agreement between the measured and predicted behaviour. It has been found that as the number of WS_2 layers increases for few-layer crystals or nanotubes, the A_{1g} mode hardens whereas the $E_{2g}{}^1$ mode softens. This is believed to be due to the A_{1g} mode, which involves out of plane atomic movements, being constrained by the increasing number of WS_2 layers whereas easy sliding reduces stress transfer to the individual layers for the $E_{2g}{}^1$ mode, involving only in-plane vibrations. This finding has enabled the anomalous phonon shift behaviour in earlier pressure measurements on WS_2 to be resolved, as well as similar effects in other transition metal dichalcogenides, such as molybdenum disulfide, to be explained.

Introduction

Tungsten disulfide (WS_2)

Transition metal dichalcogenides (TMDs) have been used widely as solid lubricants [1] and chemical catalysts [2] for many years. Interest in them has, however, grown rapidly over recent years with the explosion of research into 2D materials. This is because TMDs, unlike graphene, have a tuneable bandgap, a transition from an indirect to a direct bandgap with a reducing number of layers [3, 4] and strong spin–orbit coupling arising from broken inversion symmetry [5]. These particular properties have made TMDs very promising candidates for opto-electronic and electro-mechanical applications. The class of materials is usually expressed as MX_2, where M is a transition metal atom, such as Mo, W, Nb, etc and X represents a chalcogen atom, for instance S, Se, etc. Although the number of known combinations of MX_2 has exceeded 40 species, not all of them are of particular interest. Some are unstable under ambient conditions, react rapidly with the atmosphere and thus lose their special properties [6]. Hence, most research has focused upon the limited number of stable materials that includes WS_2, molybdenum disulfide (MoS_2), WSe_2 and $MoSe_2$. Among this group of

materials, WS_2 has drawn particular attention as a result of its unique optical [7], thermal [8] and electronic [9] properties.

The crystal structure of WS_2 involves the stacking of sheets consisting of W atoms sandwiched by two planes of S atoms packed into an individual layer of WS_2. In contrast to graphene, WS_2 exhibits a variety of polymorphs where tungsten atoms are covalently bonded to six adjacent sulfur atoms with their coordination as either trigonal prismatic or octahedral (sometimes referred to as trigonal-antiprismatic). In terms of the stacking sequence, the most extensively studied polymorphs are 2H- and 3R-WS_2 where H and R represent hexagonal and rhombohedral forms respectively and the digits denote the numbers of layers in the unit cell. The individual layers are held together through weak van de Waals forces that result in the application of TMDs as solid lubricants, similar to graphite. As the result of thermodynamic factors, the 2H stacking sequence is the most commonly-encountered crystalline form of WS_2 [10]. It belongs to the $P6_3/mmc$ space group with lattice parameters of $\mathbf{a} = 0.31532$ nm and $\mathbf{c} = 1.2323$ nm measured by x-ray diffraction [11].

Analogous to graphene, which is considered to be the building block of other sp^2 carbon allotropes, WS_2 is also found in different morphological forms such as inorganic fullerene-like nanoparticles and inorganic WS_2 nanotubes. The WS_2 nanotubes are generally considered to consist of a number of layers of WS_2 nanosheets wrapped into a 1D tubular form. They are found mostly as multiwall nanotubes, similar to those of MoS_2, with the number of sheets in the shells normally greater than four [12]. It was not until 2001 that Whitby *et al* [13] managed to synthesize single-wall WS_2 nanotubes by employing multiwall carbon nanotubes as a template. Recently single- to three-wall nanotubes of WS_2 were synthesized by high power plasma irradiation of multiwall nanotubes [14]. The difficulty of producing single-wall WS_2 nanotubes was attributed to the poor stability of single-wall materials [12] and the need for highly exergonic conditions during the reaction [14]. The inter-shell distance of multiwall WS_2 nanotubes is found to be constant throughout the walls and similar to or slightly higher [15] that of multi-layered WS_2 ($\mathbf{c}/2$). Regardless of the number of layers, the inner diameter varies over the range ~6 to ~12 nm. It has a value close to 7 nm for shell numbers less than 10 and a value of the order of 10–12 nm for shell numbers above 10, as the result of strain energy effects resulting from curvature of the WS_2 layers [12].

Preparation methods

As the result of the layer-dependent properties of WS_2, a number of different techniques have been employed to prepare exfoliated WS_2. The 'Scotch tape' mechanical exfoliation technique developed initially for the preparation of graphene is still exploited extensively in TMD research. It is the most efficient and straightforward preparation method and the specimens produced via this method possess a pristine structure that is ideal for fundamental studies of their intrinsic properties [16]. Monolayer WS_2 flakes can usually be identified and located using optical microscopy [17]. Despite the high efficiency and viability of the technique, it is difficult to scale up. Consequently this limits its use for the preparation of large quantities of material. Additionally, compared to MoS_2, crystals of WS_2 seem to be more difficult to exfoliate with this approach [18].

Another top-down preparation method is liquid phase exfoliation, where monolayer WS_2 can be obtained through sonication treatment in appropriate organic solvents [19] or aqueous solvent with aid of various surfactants [19]. This is a promising way to produce a large quantity of exfoliated WS_2 nanosheets and the resulting suspension is convenient for producing nanocomposites, thin films and coatings. Nevertheless, some applications of such products may be limited because the typical lateral size of monolayers produced by this method is only a few hundred nm [19] and larger flake sizes (typically >1 μm) are needed some applications, such as nanocomposites. A more viable method is intercalation that reduces the exfoliation barrier by intercalating ionic species into the interlayer spaces [19, 20]. This was firstly demonstrated on TMDs using lithium by Danis *et al* in 1972 [21] and later, was used to obtain monolayer of MoS_2 by Morrison *et al* in 1986 [22].

Electronic properties

The electronic structures of TMD materials have been studied extensively using first principles calculations or tight-binding approximations and characterised with a variety of spectroscopic tools [23–25]. WS_2, a typical member of the TMDs MS_2 family, shows semiconducting behaviour under ambient conditions similar to MoS_2. There is strong interlayer coupling in WS_2 and it undergoes a significant transition from an indirect band gap to a direct one with a decreasing numbers of layers [23]. Similar to graphene and other semiconductors, the mobility of the carriers in 2D TMDs including WS_2 is governed mainly by the following scattering processes: (1) acoustic and optical phonon scattering; (2) Coulomb scattering at charged impurities; (3) surface interface phonon scattering and roughness scattering [26–29].

Due to its superb electrical mobility and massless carrier properties people have sought to use graphene in different electronic devices, especially in transistors. However, the absence of a bandgap essentially makes graphene unsuitable for applications such as digital logic transistors. Semiconducting TMDs materials, including WS_2, with a sizable bandgap and high carrier mobility have therefore become very attractive for use

in transistors. Since the electronic properties of WS_2 are very layer dependent, people have examined the properties of WS_2 over a range of layer thicknesses. The transition from an indirect to a direct bandgap found on reducing the number of layers of WS_2 leads to an intense single peak profile observed in the photoluminescence (PL) spectrum of monolayer WS_2 [3, 30, 31]. This strong PL is a characteristic feature of monolayer WS_2 and has been used widely to determine the layer number, quality and uniformity of WS_2 materials.

Raman spectroscopy

Raman spectroscopy is a powerful and versatile tool to study 2D materials such as graphene and 2D TMDs. It has been used widely in probing structural information such as the number of layers, defects, doping levels, strain effects and other factors. Similar to MoS_2, bulk WS_2 belongs to the D6h point group, exhibiting A_{1g}, $2A_{2u}$, $2B_{2g}$, B_{1u}, E_{1g}, $2E_{1u}$, $2E_{2g}$ and E_{2u} vibrational modes, where only the A_{1g}, E_{1g} and $2E_{2g}$ modes are Raman active [32, 33]. In monolayer WS_2, the unit cell is composed of three atoms with nine vibrational modes at the Γ–point based on D_{3h} symmetry, which are namely $2A_2''$, A_1', $2E'$ and E''. Among these modes, the A_2'' mode is infrared active, A_1' and E'' are Raman active and E' is both Raman and infrared active. In this work, the same terminology will be used for these in monolayer and in the bulk as is commonly done in the literature [5, 7, 34–36]. In the back scattering configuration of Raman spectroscopy, the E_{1g} mode is forbidden. The $E_{2g}{}^2$ mode, also referred to as a shear mode, is found at very low frequency and usually blocked by the notch filter [37]. Therefore, $E_{2g}{}^1$ and A_{1g} are the most significant modes found in WS_2 Raman spectra.

The Raman spectrum of bulk WS_2, using a 514 nm laser excitation, comprises two major bands corresponding to $E_{2g}{}^1$ at ~351 cm^{-1} and A_{1g} at ~420 cm^{-1}. Due to the heavier mass of the W atom, the phonon bands in WS_2 are shifted to lower frequencies in comparison to MoS_2 [35]. Together with the major bands, a rich spectrum of second order bands is also observed. These second-order Raman features are seldom studied due to band overlap. For example, the longitudinal acoustic phonon mode (2LA) is very close to the $E_{2g}{}^1$ band (within ~5 cm^{-1}), causing ambiguity in investigations of the $E_{2g}{}^1$ mode [38]. Only recently, studies were conducted focusing on the 2LA mode in terms of its polarisation dependence and the effect of layer number [36, 38]. Regarding WS_2 nanotubes, the spectra show no significant differences or additional peaks when compared with the bulk materials. Only minor shifts in the position of the $E_{2g}{}^1$ and A_{1g} bands have been found due to strain effects [39]. Staiger *et al* [40] also pointed out the presence of an emerging B_{1u} mode in WS_2 nanotubes, that is silent in bulk crystals, and explored its relationship with the nanotube geometry and excitation energy.

As bulk WS_2 is thinned down to monolayer, the phonon modes are expected to soften due to the decreasing number of layers weakening the interlayer interactions [38, 41]. This indeed is the case for the A_{1g} mode where, from bulk to monolayer, a red-shift of ~3 cm^{-1} occurs. In contrast, an anomalous phenomenon has been found for the $E_{2g}{}^1$ band, where a minor blue-shift (~0.5 cm^{-1}) is observed for monolayer [41]. Similar behaviour is also observed in MoS_2 and other TMDs [41, 42]. Such anomalous behaviour allows Raman spectroscopy to be utilized as a characterisation method for the number of layers in WS_2 [36, 38]. In addition to the band shifts discussed above, the intensity ratio of the modes $E_{2g}{}^1/A_{1g}$ shows a layer dependence which varies slightly with laser excitation. Molina-Sánchez *et al* calibrated the number of layers using vibrational frequency differences, mostly between A_{1g} and $E_{2g}{}^1$ bands [35]. It should be noted, however, that none of these methods alone is absolutely reliable due to subtle shifts of the $E_{2g}{}^1$ and A_{1g} peaks and interferences brought about by adjacent second-order bands in WS_2. Overall, it is better to use them in conjunction with other characterisation methods such as atomic force microscopy (AFM) and TEM.

The Raman spectra of TMDs are very sensitive to external perturbations such as temperature, strain and magnetic fields. Several groups have undertaken research into the effects of these factors, particularly strain, on the electronic structure, phonon vibrational modes and interaction of phonons and electrons in TMDs using Raman spectroscopy [43–49]. The majority of the studies have been undertaken on MoS_2 which gives well-defined band shifts under strain. Rice *et al* [46] reported uniaxial strain induced phonon softening in monolayer and few-layer MoS_2. They found shift rates of -0.4 cm^{-1}/% strain for the A_{1g} mode in both mono- and few-layer crystals and -2.1 cm^{-1}/% strain, -1.7 cm^{-1}/% strain for the $E_{2g}{}^1$ mode in monolayer and few-layer crystals respectively. The $E_{2g}{}^1$ mode is believed to be more sensitive to uniaxial strain since its corresponding in-plane vibrations whereas the A_{1g} mode is perpendicular to the crystal plane. Moreover, a splitting of the $E_{2g}{}^1$ mode was observed in a similar experiment when strained up to 0.8%, indicating the removal of degeneracy arising from the breaking of symmetry by strain [45, 47]. In addition, Nayak *et al* demonstrated a pressure-induced semiconducting-to-metallic transition in few-layer MoS_2 using ultra-high hydrostatic pressure (35 GPa) indicating the successful modulation of electronic structure with strain [43]. A similar pressure-induced transition was later achieved in few-layer WS_2, showing similar behaviour to MoS_2 [44]. Similar levels of stress-induced Raman band shifts were predicted for both MoS_2 and WS_2 nanotubes by Ghorbani-Asl and coworkers [49]. Recently, a detailed study has been undertaken of the high-pressure vibrational properties of WS_2 nanotubes using

synchrotron-based infrared and Raman spectroscopies [48]. It was found that most of the vibrational modes showed a similar hardening trend with their vibrational frequencies increasing with pressure, with the exception of the A_{1g} mode which exhibited strong pressure sensitivity.

Mechanical properties

The number of investigations that have been undertaken upon the intrinsic mechanical properties of WS_2 is very limited. Initial experiments were undertaken upon WS_2 nanotubes using a very delicate methodology developed for the study of carbon nanotubes where AFM and *in situ* scanning electron microscopy (SEM) were used synchronously to determine stress and strain, as well as to gain an insight into the deformation process [50–52]. It is found that WS_2 exhibits a high value of Young's modulus in range of 150–170 GPa, a shear modulus of 2 GPa, a high strength of ~16 GPa and an impressive fracture strain at 14%. This value of Young's modulus is in good agreement with theoretical predictions, implying a low level of defects [51]. The good performance of WS_2 nanotubes is comparable to that of strong conventional materials such as steel, aramid fibres and some classes of carbon fibres. In particular, however, the 14% strain to failure is a feature unique to all nanotube materials [50]. People have also conducted pressure studies on bulk WS_2 using x-ray diffraction to monitor changes in the **a** and **c** lattice parameters [53]. The bulk modulus was determined to be $K_{0T} = 61 \pm 1$ GPa with $K'_{0T} = 9.0 \pm 0.3$ GPa. Furthermore, the **c**-direction of the hexagonal crystal structure was found to be much more compressible than the **a**-direction. With research interest sparked into 2D TMDs, their intrinsic mechanical properties have been investigated more recently [54, 55]. Liu *et al* [54] studied the elastic properties of WS_2, MoS_2, graphene and their bilayer heterostructures(in the **a**–**b** plane). It was found that the 2D moduli of MoS_2 and WS_2 are very close, giving values of 171 ± 11 N m^{-1} and 177 ± 12 N m^{-1} respectively, half of that of graphene (349 ± 12 N m^{-1}).

The present study aims to understand the structure-property relationships in the different forms of WS_2. This has been undertaken by firstly characterising the structural similarities and differences between the structure and properties of exfoliated monolayer and few-layer WS_2 nanoplatelets, and WS_2 nanotubes using a combination of high-resolution TEM and Raman spectroscopy. The effect of deformation upon these materials has then been followed from strain-induced Raman bands shifts that have been related to change in the phonon modes of WS_2 crystals with deformation predicted using density functional theory.

Materials and methods

Materials

The few-layer WS_2 nanoplatelets were prepared on a Si/SiO_2 substrate by tape exfoliation from WS_2 crystals with an average grain size of 200 μm supplied by HQ Graphene, Groningen, the Netherlands. An AFM (Bruker Dimension 3100) operated in the tapping mode was used to determine the thickness of the exfoliated WS_2 nanoplatelets on the Si/SiO_2 substrate. The WS_2 nanoplatelets were also examined by SEM (Philip XL30 FEG-SEM) using an accelerating voltage of 8 kV on the Si/SiO_2 substrate after coating with gold to reduce charging.

The WS_2 nanotube samples were synthesized by a bottom-up solid–gas reaction for which the detailed growth reaction is given in another publication [56]. In this processs, tungsten oxide nanoparticles of ~100 nm in diameter were used as a precursor to react with hydrogen (H_2) and hydrogen sulfide (H_2S) gases at a temperature of 750°C–840 °C. The reaction proceeds in a one pot mode from the growth of suboxide nanowhiskers to beyond full oxide-to-sulfide conversion and the formation of hollow WS_2 nanotubes. The technique can produce nanotubes with different dimensions but in this study we have confined our investigations to thick (50–150 nm) and long (micron dimensions) nanotubes consisting of many (>20) layers.

Similar characterisation techniques as those used for the WS_2 nanoplatelets (SEM and AFM using the same instruments) were employed to characterise the morphology of the nanotubes. A nanotube/acetone suspension was prepared using a 30 min sonication bath to break the bundles and achieve a homogenous suspension. The SEM and AFM specimens were then produced by drop casting the nanotube/acetone suspension on to a Si/SiO_2 substrate and characterised in the same way as the WS_2 nanoplatelets described above.

Transmission electron microscopy

The WS_2 nanoplatelets were exfoliated onto a Si/SiO_2 substrate as described above. The deposited flakes were then transferred to a lacey carbon Cu TEM grid via a polymer-free technique. The nanotubes were prepared by sonication in de-ionised water for 15 min before being dropped via a micropipette onto a Cu quantifoil TEM grid. The solution was left to dry on a hot plate for 5 min at 100 °C. The TEM used during this project was a JEOL 2100 field emission TEM, operated at an accelerating voltage of 200 kV. All TEM images were taken using phase contrast imaging in a bright field detector, with acquisition times between 0.5 and 2.5 s.

Raman and PL spectroscopy

Raman spectroscopy employing a laser excitation of 514 nm was used initially to characterise the structure

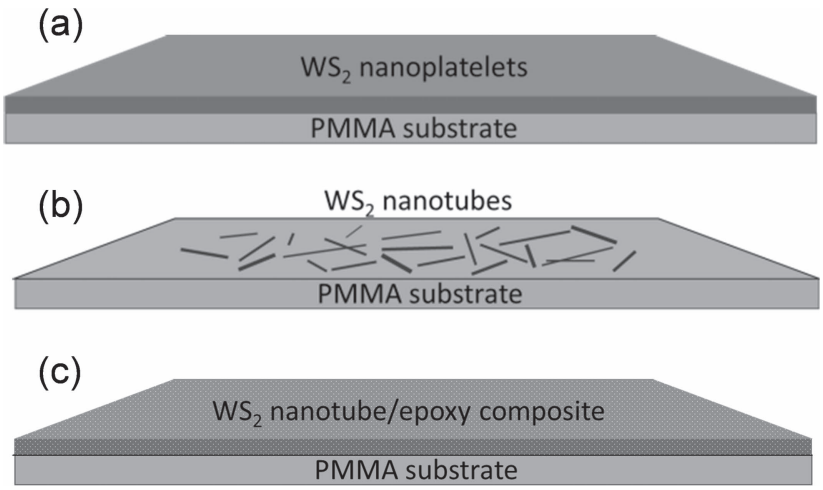

Figure 1. Schematic diagrams of the three different types of PMMA beam prepared for deformation studies. (a) Exfoliated WS_2 monolayer or few-layer nanoplatelets on the beam surface. (b) WS_2 nanotubes dispersed on the beam surface. (c) WS_2 nanotubes in an epoxy resin matrix spun cast onto the beam surface.

of the WS_2 nanoplatelets and nanotubes on Si/SiO_2 substrates. The specimens that were employed in the Raman experiments were also used for the AFM studies. Spectra were obtained using a Renishaw 1000 Raman spectrometer with a 50x objective lens giving a laser spot size of the order of 1–2 μm. To prevent radiation damage and undue specimen heating the power of the laser beam kept below 1 mW. PL spectroscopy was employed in order to identify monolayer regions in thin exfoliated crystals using a Horiba LabRAM HR Evolution spectrometer with the 488 nm line of an argon ion laser.

In situ deformation studies were undertaken in the same Raman spectrometer. In this case the WS_2 nanoplatelets and nanotubes were deformed on the surfaces of a poly(methyl methacrylate) PMMA beams. The WS_2 nanoplatelets were transferred to the PMMA beam surface after mechanical tape exfoliation from the WS_2 crystals and deformed without the application of any further coating. In the case of the WS_2 nanotubes, they were drop casted onto the PMMA beam surface from a nanotube/ethanol suspension and then first deformed on the beam with no top coat of resin. Subsequently, a WS_2-nanotube/epoxy solution with a nanotube loading of 0.5 wt% (relative to the epoxy resin) was prepared and spin coated onto a PMMA beam coating and then allowed to cure for 24 h at room temperature. The three different types of specimen used in the deformation studies are shown schematically in figure 1 and the experimental set-up is illustrated in figure S1 of the supporting information.

The PMMA beams were deformed using the four-point bending rig on the specimen stage of the Raman spectrometer with the direction of laser polarisation parallel to the tensile axis. The position of different WS_2 Raman bands from the nanoplatelets and nanotubes was determined as a function of strain. Spectra were obtained from the centre of the nanoplatelets and from individual nanotubes lying in a direction parallel to the tensile axis. A resistance strain gauge linked to a multimeter was attached to the tensile surface of the beams to monitor the strain on the beam surface. As the thickness of the WS_2 nanomaterials was several orders of magnitude thinner than the PMMA beam, bending the beam led essentially to the application of uniaxial strain through the PMMA substrate using the bending rig. The strain was capped at around 0.5% to avoid damage to the polymer-WS_2 interface. Similar band shift behaviour was observed after several strain cycles, indicating an intact interface.

Density functional theory

Ab initio methods have been very successful at reproducing the measured phonon dispersion of MoS_2 [57] hence we used first-principles plane-wave calculations based on density functional perturbation theory (DFPT) [58] to calculate the frequencies of the phonon modes at the Brillouin zone centre as a function of in-plane strain. We used DFPT as implemented in the QUANTUM ESPRESSO package [59] with ultrasoft pseudopotentials [60]; the $5s^2$, $5p^6$, $5d^4$ and $6s^2$ electrons of W were treated as valence electrons, giving a total valence of 14 for W. The local density approximation (LDA) was used with a Perdew–Zunger exchange-correlation functional [61], as the LDA was found satisfactory in earlier studies [62]. Layers in the three-dimensional supercell were spaced by about 1 nm to ensure there was no interaction between them and so no van der Waals corrections were required. Convergence of the total energy was checked with respect to the kinetic energy cutoff (60 Ry) and Brillouin zone sampling (an $18 \times 18 \times 1$ Monkhorst–Pack grid was used) [63]. The optimized lattice parameter **a** was found to be 0.3122 nm, which

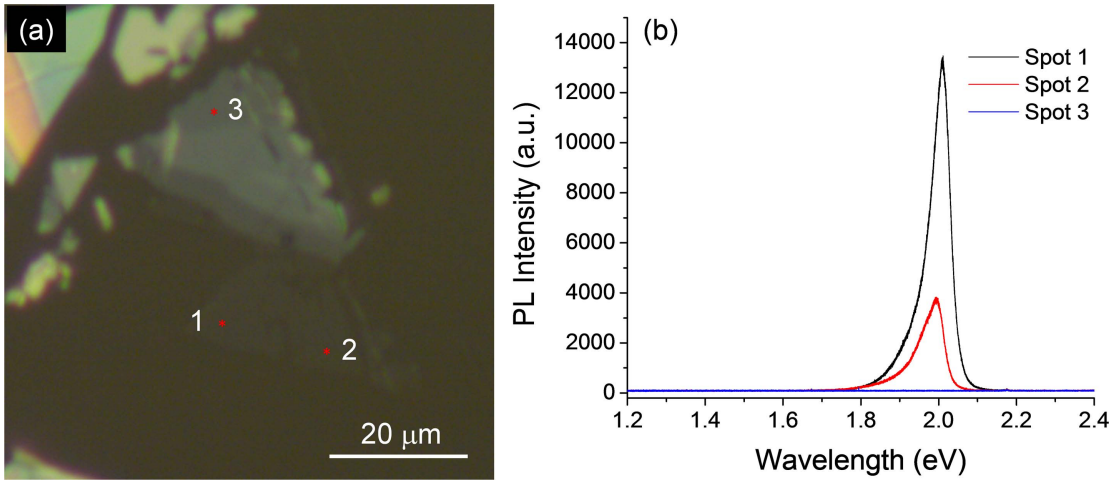

Figure 2. (a) Optical micrograph of exfoliated WS_2 nanoplatelets. (b) PL spectra obtained from different positions shown in the micrograph, showing stong PL from region 1 (monolayer).

agrees to better than 1% with the experimental value of 0.315 32 nm [11].

Two types of distortion of the planar lattice were applied; a symmetry-preserving isotropic expansion ('hydrostatic') and a shear distortion ('shear'), which preserves area [64]. In both cases, the positions of the W atoms were fixed to obtain the required unit cell parameters but the S atoms were allowed to relax in the direction normal to the layer plane to minimize the vertical forces on them before calculation of the lattice modes (these forces were always less than 10^{-4} eV $Å^{-1}$). The maximum strains used were of the order of 0.5% and so no adjustment to the density of *k*-point sampling was necessary.

Results

Structure and morphology

Nanoplatelets produced by the tape exfoliation normally have a range of number of layers and require the aid of optical microscopy and AFM to locate and identify them [65, 66]. Monolayer WS_2 was more difficult to locate using optical microscopy and AFM and so PL spectroscopy [3] was also employed. Figure 2(a) shows an optical micrograph of flakes with regions of different thickness and the positions where PL spectra were obtained are marked. It can be seen from figure 2(b) that a very strong PL peak at 2 eV is obtained from position 1 indicating that this is an area of monolayer WS_2 [3].

Analysis of a number of SEM images shows the resulting flake size ranges ranging from a few microns to tens of microns (figure 3(a)), with some evidence of folding. In contrast to graphene, this is considerably smaller after mechanical exfoliation than the original crystal size in the starting materials (~1 mm), probably due to the poorer mechanical properties of WS_2 compared to graphene [52, 54]. The optical micrograph of a flake in figure 3(b) illustrates a small nanoplatelet (highlighted) that had a characteristic blue colouration which is a fingerprint for a thin WS_2 nanoplatelet in the optical microscope [67] with AFM confirming its height as a ~5.6 nm step corresponding to a few-layer nanoplatelet with around 9 WS_2 layers (figure 3(c)).

Figure 4(a) shows the WS_2 nanotubes dispersed on a Si/SiO_2 substrate, where the NTs are oriented randomly and can be seen to stack together to form bundles. A high magnification image of an individual NT is shown in figure 4(b) and the open-tip nature of this WS_2 NT is evident as reported earlier [68]. The outer diameter given by the AFM measurement of the NT in figure 4(b) was measured as 43 nm. It was found that the outer diameter of NTs was in the range 20–200 nm consistent with the reported values [56]. Further analysis of the length of the NTs in figure 4(a) using image analysis software is given figure 4(c). It shows that the length distribution of the NTs is in the range 0.3 – 10 μm with the majority being shorter than 2 μm, again consistent with the reported values [56]. However, no careful analysis of the influence of the ultrasonic (US) treatment on the length of the nanotubes was undertaken. Typically, a mild US treatment leads to breakage of the nanotubes and to an average shortening by a factor of 2.

Transmission electron microscopy

Figure 5(a) shows a low magnification bright field TEM image of an exfoliated WS_2 nanoplatelet on a lacey carbon Cu grid. The flake is folded and a number of few-layer regions were located at the edges. One such region is presented in figure 5(b). The number of layers decreases from left to right, as indicated in the intensity profile taken along the arrow. We estimate the thinnest region contains 2–3 WS_2 layers. This thin region is displayed in a fast Fourier transform (FFT) filtered high-resolution image in figure 5(c) (masked

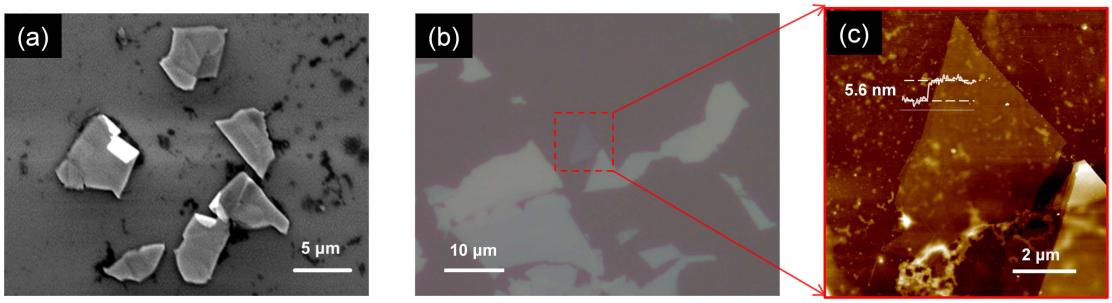

Figure 3. (a) SEM micrograph (b) optical micrograph and (c) AFM image of few-layer exfoliated WS_2 nanoplatelets showing the flake where *in situ* measurement was taken. The dark areas seen in figure 2(a) and light spots in figure 2(c) are adhesive residue from the tape used for the exfoliation.

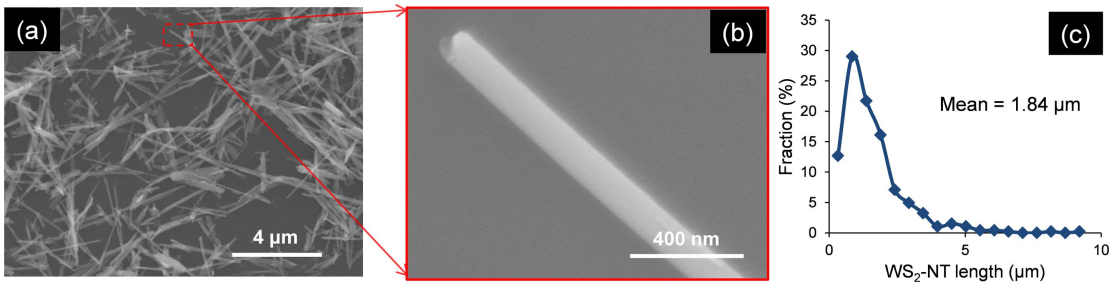

Figure 4. (a) SEM micrograph of the WS_2 nanotubes and (b) the magnified detail showing the nanotube morphology. (c) The length distribution of WS_2 nanotubes determined from the SEM micrographs using ImageJ software.

FFT inset). Contrast appears to change throughout the image, caused by undulations in the atomic lattice. These result in peaks and troughs which are highlighted in areas (i), (ii) and (iii). Area (i) shows a typical under-focused hexagonal bright field lattice (trough), indicating that area (i) is perpendicular to the zone axis. Area (ii) shows an over-focused area (peak) wherein the hexagonal structure appears white rather than black. The hexagonal structure in the top left section of (ii) and the under-focused area (iii) appear stretched, which is due to a slight tilt in the lattice, i.e. in the location between a peak and a trough.

The structure of the WS_2 nanotubes was also investigated using TEM. A low magnifcation image of the NTs is shown in figure 6(a) along with measurements of their lengths. It can be see that they are consistent with the sizes of the NTs determined in figure 4. The micrographs in figures 6(b) and (c) shows the nanotube tips and confirms that they can either be closed or open-ended. The closed tip consists of ~23 atomic layers, while the open-ended tip changes from ~22 in the body to ~10 atomic layers near the tip. A high resolution micrograph of the wall of a nanotube is shown in figure 6(d) along with an intensity scan (inset) across ~23 atomic layers. The average spacing between the peaks in the scan in of the order of 0.634 nm, slightly larger than **c**/2 in the unit cell of the bulk material [11] but comparable to the value of 0.631 nm observed in our earlier study [15].

Raman spectroscopy

Figure 7(a) shows typical Raman spectra of WS_2 NTs, a WS_2 single crystal, a WS_2 nanoplatelet and a WS_2 monolayer. As shown in figure 7(b), the $E_{2g}{}^1$ mode involves an in-phase vibration of the W atoms with respect to the S atoms vibrating in the opposite direction in-phase, while the A_{1g} mode arises from the S atoms moving in in-phase and in out-of-plane directions [45, 46]. In addition to the first-order modes, WS_2 gives a rich spectrum of second-order and multi-phonon bands with the laser excitation of 514 nm, due to strong electron–phonon coupling [38]. The 2LA mode overlaps with the $E_{2g}{}^1$ mode as the result of a very minor frequency difference (~5 cm^{-1}). The individual components can, however, be separated by curve-fitting with a Lorenzian function [38, 69]. It is noteworthy that the ratio between the two major bands is different for the single crystal, few layer and monolayer specimens. This is consistent with the report of Berkdemir *et al* [38] who showed an increase of the $I_{E^1_{2g}}/I_{A_{1g}}$ ratio in WS_2 with a decreasing number of layers. Additionally, the A_{1g} mode undergoes a very subtle red shift as the number of layers is reduced. This trend is expected due to the decrease in the interlayer van der Waals interaction, causing weaker restoring forces in the vibration as the number of layers decreases. A blue-shift was, however, found for the $E_{2g}{}^1$ mode. Such behaviour have been widely observed among TMDs (MoS_2, $TaSe_2$, WSe_2) and is attributed to the reduced long-range Coulomb interaction

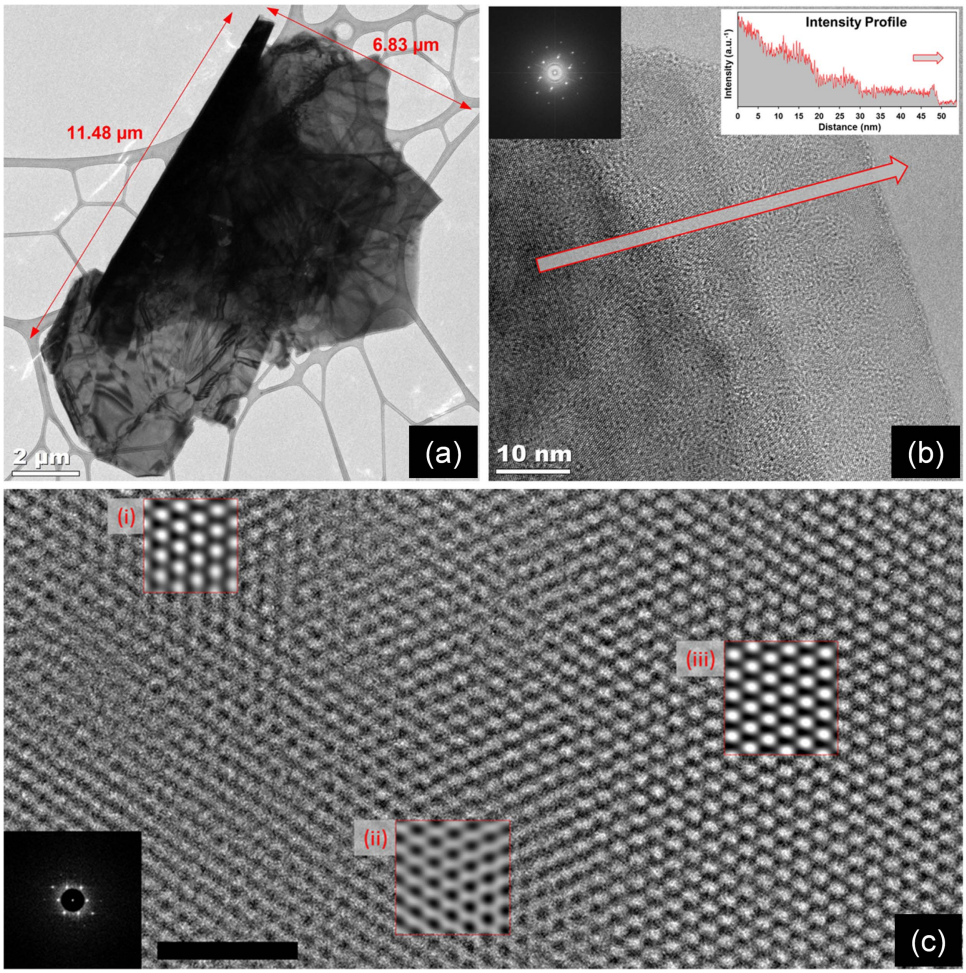

Figure 5. Bright field TEM images of a WS_2 nanoplatelet at low (a), medium (b) and high (c) magnification. Few-layer regions were identified at the edges of the nanoplatelet as seen in (b). The inset intensity profile taken along the arrow shows thinner layers from left to right. (c) FFT filtered high-resolution image of the thinnest region from (b), with masked FFT inset. The differences in image contrast throughout are due to sample undulations, resulting in peaks and troughs. These are highlighted in three areas: (i) under-focused along the zone axis, (ii) over-focused with partial sample tilt and, (iii) under-focused with sample tilt (scale bar = 2 nm).

between the effective charges caused by an increase in the dielectric screening or stacking-induced changes in the intra-layer bonding [31, 46, 70]. This trend was also evident upon the thinning down of the WS_2 nanoplatelets during the exfoliation process.

Deformation

Deformation of the WS_2 nanoplatelets and nanotubes on the surface of the PMMA beam substrate was undertaken as shown schematically in figure 1 with Raman spectra being obtained *in situ*. The results of *in situ* Raman deformation measurements of the WS_2 monolayer shown in figure 2 are presented in figure 8. It is clearly seen that there is a significant red-shift in the 2LA, $E_{2g}{}^1$ and A_{1g} modes. This indicates good stress transfer as a result of a strong van der Waals interaction between the exfoliated nanoplatelets and the substrate aided by the large contact area. Similar strain-induced phonon softening has been observed in uncoated graphene nanoplatelets using the similar preparation method with uncoated specimens [71]. The band shift rates for the A_{1g}, $E_{2g}{}^1$ and 2LA Raman bands for the monolayer were $-0.58 \pm 0.07\ cm^{-1}/\%$ strain, $-2.05 \pm 0.14\ cm^{-1}/\%$ strain and $-2.07 \pm 0.19\ cm^{-1}/\%$ strain, respectively and they are listed in table 1.

The strain induced band shifts for the few-layer nanoplatelet shown in figure 3 are presented in figure 9 and the shift rates of the A_{1g}, $E_{2g}{}^1$ and 2LA Raman bands are listed in table 1. The lower shift rates for the $E_{2g}{}^1$ and 2LA Raman bands are an indication of slippage between the WS_2 layers. This is due to difficulties in stress transfer as the result of the weak van der Waal bonding between the layers as has been found in few-layer graphene [72]. On the other hand the shift rate is higher than in the monolayer for the A_{1g} band; this anomalous behaviour will be discussed later.

The results of the *in situ* Raman measurement on the uncoated WS_2 NT specimen are shown in figure 10(a). In this case there is no measureable shift in any of the three Raman bands as the result of the absence of stress transfer due to poor contact between the nanotubes and substrate. Their cylindrical nature (figure 4) means that the contact area is minimal and,

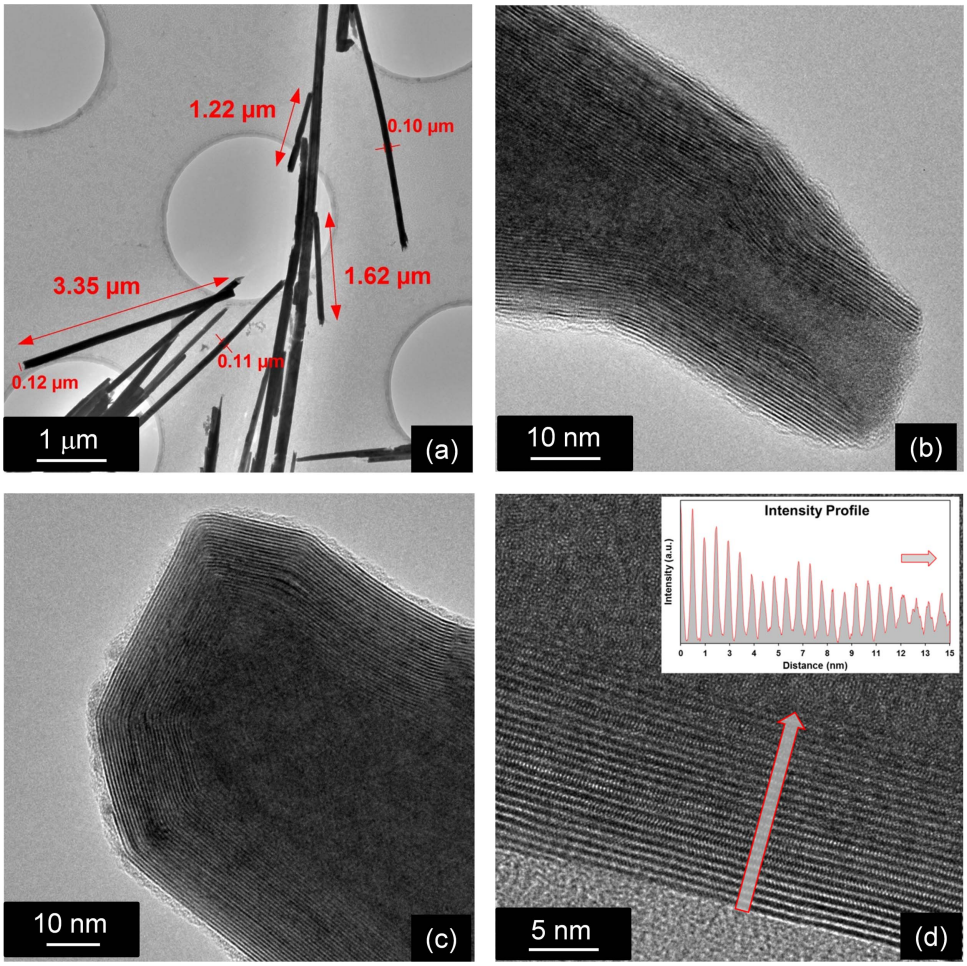

Figure 6. (a) Low magnification TEM image of a cluster of WS_2 nanotubes (NT) with dimensions consistant with those determined in figure 4. An open (b) and closed (c) NT tip confirming that WS_2 can exist in either state. (d) High-resolution micrograph of a NT wall with an intensity profile inset along the direction of the arrow. The 15 nm intensity profile contains ~23 atomic layers with an average layer distance of 0.634 nm, slightly higher than the **c**/2 unit cell value.

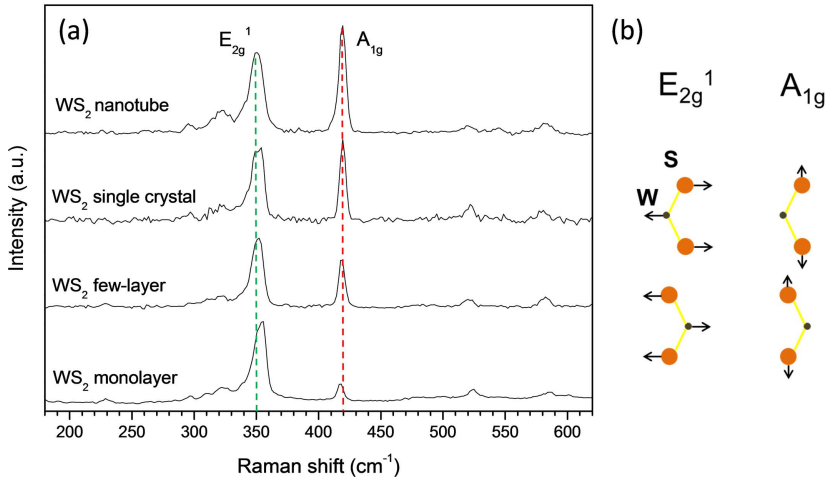

Figure 7. (a) Raman spectra of WS_2 NTs, a WS_2 single crystal, a few-layer WS_2 nanoplatelet and monolayer WS_2. The vertical broken lines allow comparison of the positions of the A_{1g} and E_{2g}^1 bands in the different materials. (b) Atomic displacements in the two Raman active modes of 2H–WS_2.

moreover, the fact that the nanotubes have steps in their walls and are not completely straight (figure 6) makes the contact with the substrate even more difficult. Figure 10(b) shows that the behaviour is completely different for the WS_2 NTs in the epoxy resin. In this case large band shifts are found for all

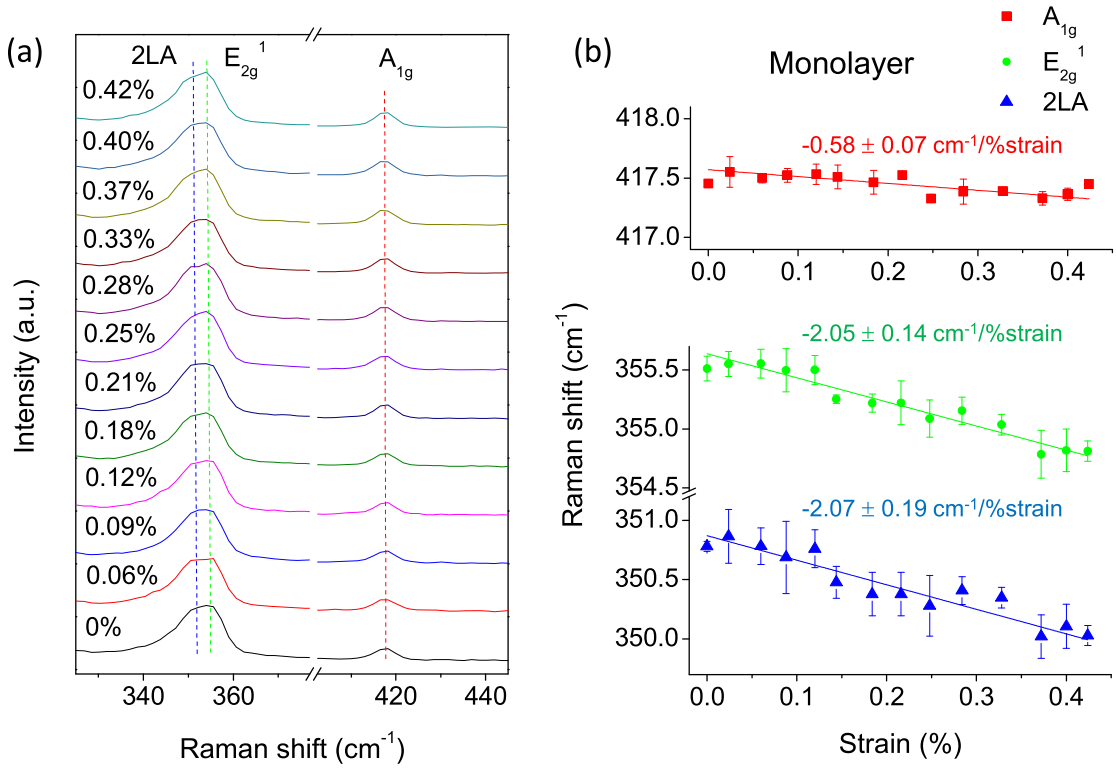

Figure 8. (a) Shift of the A_{1g}, E_{2g}^1 and 2LA Raman modes during the deformation a WS_2 monolayer nanoplatelet on a PMMA bending specimen deformed to the different levels of strain indicated. (b) Raman frequencies of A_{1g}, E_{2g}^1 and 2LA bands as a function of strain. The solid lines are the linear fits of the data.

Table 1. Raman band positions and band shift rates determined for three main bands in the different specimens of WS_2 exfoliated monolayer and few-layer nanoplatelets, and nanotubes.

Specimen	A_{1g} (cm^{-1})	$\partial\omega(A_{1g})/\partial\varepsilon$ (cm^{-1}/% strain)	E^1_{2g} (cm^{-1})	$\partial\omega(E^1_{2g})/\partial\varepsilon$ (cm^{-1}/% strain)	$\partial\omega(2LA)/\partial\varepsilon$ (cm^{-1}/% strain)
Monolayer (uncoated)	417.6	−0.58 ± 0.07	355.6	−2.05 ± 0.14	−2.07 ± 0.19
Few-layer (uncoated)	419.0	−0.74 ± 0.05	354.5	−1.03 ± 0.18	−1.15 ± 0.36
Nanotubes (uncoated)	420.9	~0	354.9	~0	~0
Nanotubes (composite)	421.3	−1.73 ± 0.11	355.6	−1.60 ± 0.17	−2.29 ± 0.24
Calculated (DFPT)	421.7	−0.50	361.1	−2.18, −0.16	n/a

three bands as shown in the figure and listed in table 1. In particular the shift rates of the bands are similar to those for the monolayer with the exception of the A_{1g} mode which is the highest of all materials studied. The is reason for this phenomenon will be discussed later.

The Raman band shifts for monolayer WS_2 were also calculated using DFPT using an identical approach to that used for monolayer MoS_2 in our earlier publication [46]. Two types of distortions of the planar lattice were applied; a symmetry-preserving isotropic expansion and a shear distortion that preserves area [64]. In each case, the positions of the W atoms were fixed to obtain the required unit cell parameters but the S atoms were allowed to relax in the z (hydrostatic) and x, y, z (shear) directions to minimize the forces on them before calculation prior to calculating the lattice modes. The maximum strains used were the order of 0.5% so that no adjustment to the density of the k-point sampling was necessary. We followed the method of Mohiuddin *et al* [73] to derive the phonon shift for uniaxial strain. For the hydrostatic case, the symmetry modes of type E (in-plane displacements) and type A (out-of-plane displacements) shift to lower frequency ω as the lattice expands at a rate that is given by the Grüneisen parameter γ_m for a particular phonon mode m as:

$$\gamma_m = \frac{1}{\omega_m}\frac{\partial\omega_m}{\partial\varepsilon}, \qquad (1)$$

where the strain $\varepsilon = \varepsilon_x + \varepsilon_y$. Further details of the analysis are given in our earlier publication [46]. The frequency values calculated by DFPT for the A_{1g} and E_{2g}^1 modes are compared to the experimentally measured values of in table 1 and it can be seen that there is a good agreement between the calculated and measured frequencies for the monolayer and few-layer nanoplatelets, and nanotubes giving confidence in our DFPT calculations. Our values of the Grüneisen

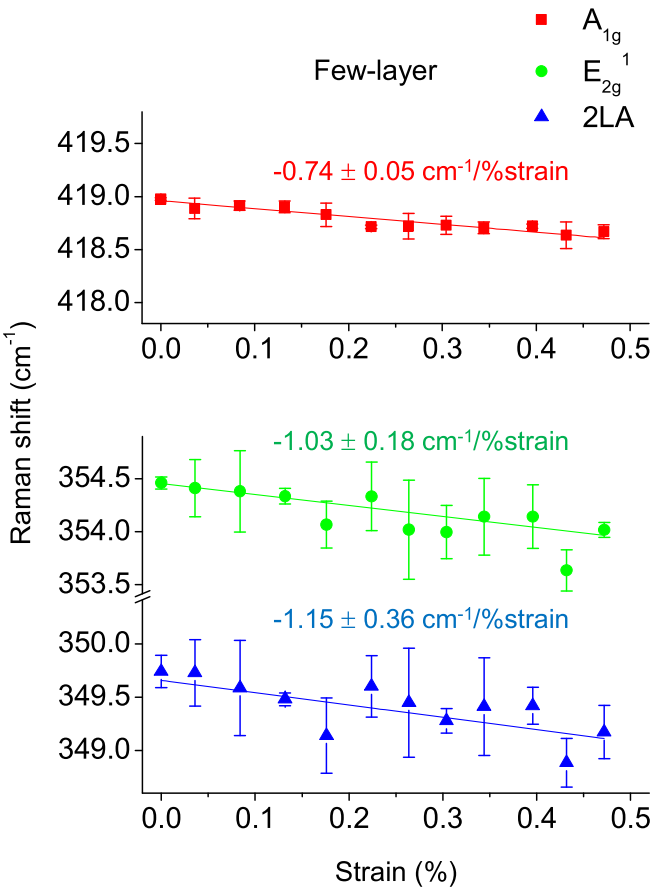

Figure 9. Shift of the A_{1g}, $E_{2g}{}^{1}$ and 2LA Raman modes during the deformation a few-layer WS_2 nanoplatelet showing the Raman frequencies of the bands as a function of strain. The solid lines are the linear fits of the data.

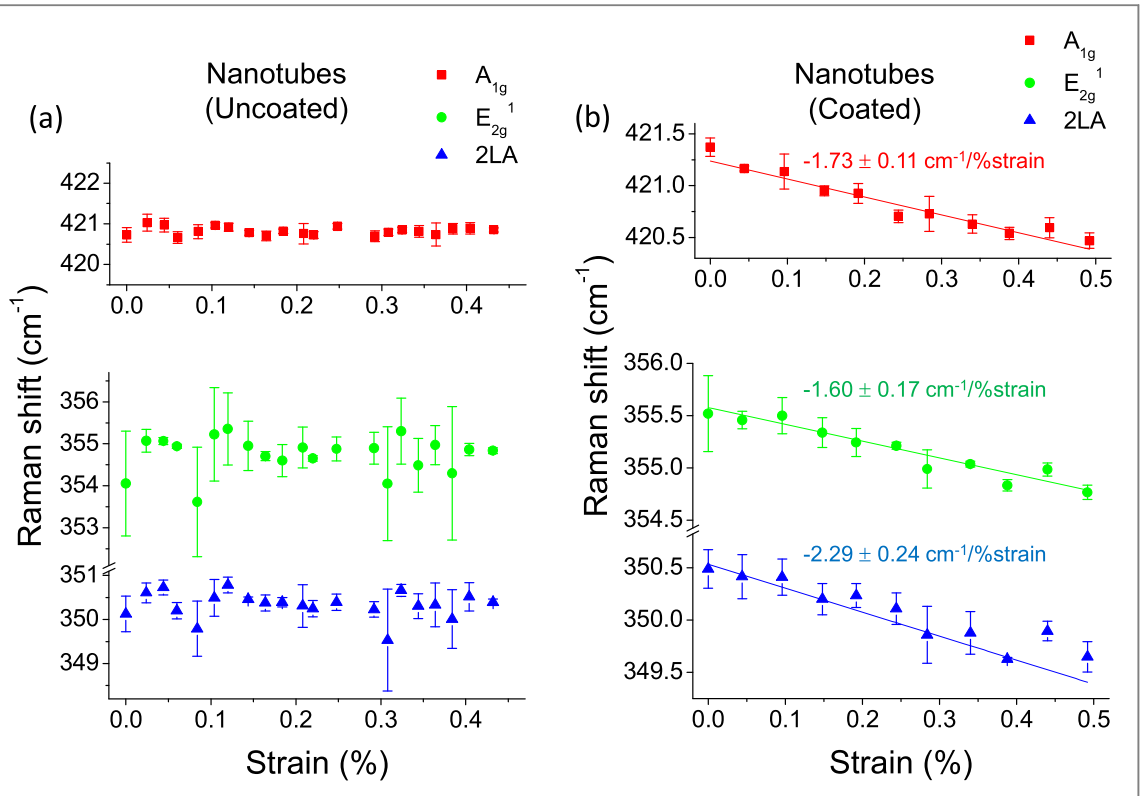

Figure 10. (a) Behaviour of the A_{1g}, $E_{2g}{}^{1}$ and 2LA Raman modes during the deformation of a PMMA bending specimen deformed to the different levels of strain indicated with (a) uncoated WS_2 nanotubes and (b) WS_2 nanotubes coated in an epoxy resin matrix.

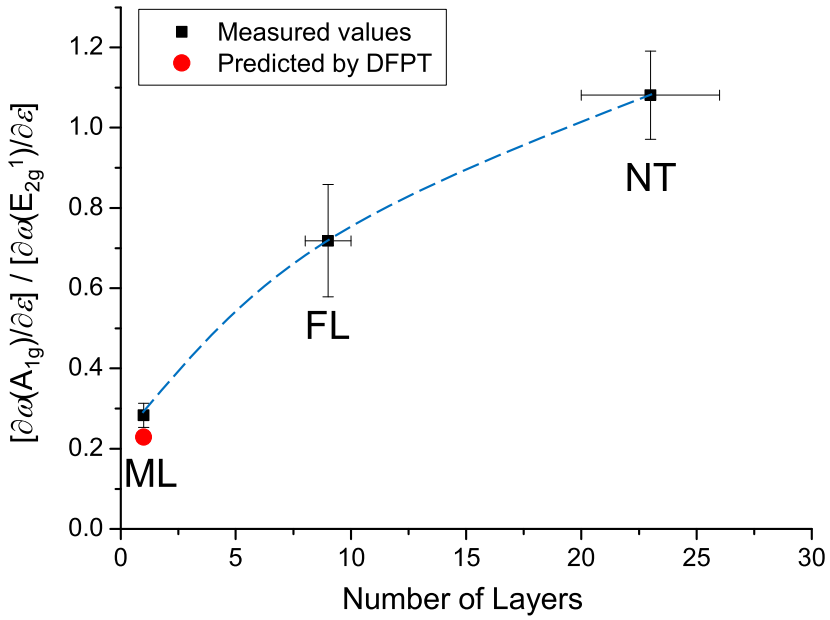

Figure 11. Variation of the measured value of the ratio of the Raman band shift rates $[\partial\omega(A_{1g})/\partial\varepsilon]/[\partial\omega(E_{2g}{}^1)/\partial\varepsilon]$ with the number of layers for WS_2 monolayer (ML), few-layer (FL) nanoplatelets and nanotubes (NT). The value predicted for the monolayer from DFPT is also indicated.

parameters $\gamma_{A_{1g}}$ and $\gamma_{E^1_{2g}}$ calculated for the WS_2 monolayer were 0.18 and 0.50 respectively.

Discussion

The calculated values of the Raman band shift rates determined from the Grüneisen parameters for the A_{1g} and $E_{2g}{}^1$ modes in the monolayer are also listed in table 1. It can be seen that good agreement is obtained between the measured and calculated values for the monolayer. Significant discrepancies between the measured and calculated values of Raman band shift rates and Grüneisen parameters are found, however, for the few-layer nanoplatelets and nanotubes. In particular the value of $\partial\omega(A_{1g})/\partial\varepsilon$ is found to be higher and the value of $\partial\omega(E^1_{2g})/\partial\varepsilon$ lower, respectively, for the few-layer nanoplatelets and nanotubes than for the monolayer. This is shown more clearly in figure 11 where the ratio of the two shift rates plotted against the number of layers in the WS_2 nanostructures. It can be seen that there is a large and systematic change for the WS_2 crystals with different morphologies. The reasons for this behaviour will now be considered. Firstly, there is a significant increase in the value of $\partial\omega(A_{1g})/\partial\varepsilon$ as the number of layers increases indicating hardening of the mode. This mode involves out-of-plane atomic motion (figure 7(b)) and is therefore sensitive to the number of layer present in the crystal. Secondly, the $E_{2g}{}^1$ mode involves only in plane atomic motion and is not hardened by the increase in the number of layers. The value of $\partial\omega(E^1_{2g})/\partial\varepsilon$ actually decreases as the number of layers increases due probably to poor stress transfer from the substrate through the crystal, due to easy shear, as has been found for few-layer graphene [72, 74]. These findings are consistent with recent studies upon multilayer WS_2 [44] and WS_2 nanotubes [48] deformed under pressure where in both cases significantly higher Raman band shift rates with pressure were found for the A_{1g} mode than for the $E_{2g}{}^1$ mode.

It is known from the behaviour of graphene [74] that stress-induced Raman band shifts can be used to estimate the effective Young's modulus of forms of graphene with different numbers of layers. The measured value of $\partial\omega(E^1_{2g})/\partial\varepsilon$ enables the relative in-plane Young's modulus of the different WS_2 nanomaterials to be estimated in a similar way. Since the measured value for the WS_2 monolayer predicted is similar to that predicted using DFTP theory, it is likely that the monolayer has the theoretical modulus value of 150–170 GPa. The value of $\partial\omega(E^1_{2g})/\partial\varepsilon$ for the few-layer material is around half that of the monolayer material, hence it would be expect that its Young's modulus would be half the theoretical value due to easy shear between the van der Waals bonded layers [74]. On the other hand the value of $\partial\omega(E^1_{2g})/\partial\varepsilon$ for the nanotubes is around 80% of that of the monolayer, implying a reduction in Young's modulus of around 20% compared to the monolayer.

Our present studies also enable similar observations to be explained for stress-induced phonon shifts in MoS_2 nanoplatelets. Rice *et al* [46] undertook an experimental study of phonon shifts during the uniaxial deformation of MoS_2 monolayer and few layer crystals. They found that the shift rate of the A_{1g} mode per unit strain was significantly lower than that for the $E_{2g}{}^1$ mode, an observation confirmed by their DFPT calculations for MoS_2 monolayer. In contrast, studies upon the deformation of multi-layered [43] and bulk

[75] MoS_2 crystals under pressure have shown significantly higher Raman band shift rates with pressure for the A_{1g} mode as compared with the $E_{2g}{}^1$ mode. This hardening of the A_{1g} mode with the increase in crystal thickness seem therefore to be a characteristic of crystals of 2D TMD materials showing that care must be taken in comparing and correlating the behaviour of materials with different crystal morphologies.

A related study by Conley *et al* [76] showed that PL spectroscopy could be used to follow the change in the optical band gap in monolayer and bilayer MoS_2 with strain from shifts of peak positions and intensity changes. In view of the similarities of the structure and properties of these two TMD materials it is highly likely that the PL in WS_2 will undergo similar changes with strain. Hence a combination of Raman spectroscopy and PL spectroscopy on these materials can give a unique insight into both their structure and physical properties.

Conclusions

A detailed investigation has been undertaken of strain-induced phonon shifts in tungsten disulfide monolayer and a few-layer nanoplatelet, and nanotubes. The materials were fully characterised and in all cases signficant Raman band shifts have been found for both the A_{1g} and $E_{2g}{}^1$ modes. This behaviour has been modelled using DFPT theory and good agreement between theory and experiment has been obtained for monolayers. For thicker crystals, however, the A_{1g} mode has been found to harden and the $E_{2g}{}^1$ mode to soften as the number of layers in increased. Similar behaviour is found for both few-layer material and nanotubes showing consistency between the different morphological forms of WS_2. In addition, this study has also enabled anomalous phonon shift behaviour during the deformation for MoS_2 to be explained.

Acknowledgments

This research has been supported by funding from the European Union Seventh Framework Programme under grant agreement n°604391 Graphene Flagship and the EPSRC (award no. EP/I023879/1). Computational work was performed on the High Performance Computing Facility of the University of Bath. RT and AZ acknowledge the support of the the FTA action 'Inorganic nanotube-polymer composites' No. 711543 of the Israel National Nano Initiative. The authors are also grateful to Dr Mark Bissett for his help with the preparation of monolayer crystals and photoluminescence spectroscopy.

References

[1] Baranov N G, Ageeva V S, Ilnitskaya A I, Bogaichuk N T and Fedorenko G A 1990 Structure and tribological characteristics of copper tungsten disulfide powder composite-material *Sov. Powder Metall. Met. Ceram.* **29** 832–5

[2] Bohm H, Diemer W, Heffler J, Pohl F A and Sigmund W 1970 Molybdenum disulfide and tungsten disulfide, catalysts for fuel cells *Energy Convers.* **10** 119–22

[3] Gutierrez H R *et al* 2013 Extraordinary room-temperature photoluminescence in triangular WS_2 monolayers *Nano Lett.* **13** 3447–54

[4] Yun W S, Han S W, Hong S C, Kim I G and Lee J D 2012 Thickness and strain effects on electronic structures of transition metal dichalcogenides: 2H-MX_2 semiconductors (M = Mo, W; X = S, Se, Te) *Phys. Rev.* B **85** 033305

[5] Zeng H, Dai J, Yao W, Xiao D and Cui X 2012 Valley polarization in MoS_2 monolayers by optical pumping *Nat. Nanotechnol.* **7** 490–3

[6] Bosi M 2015 Growth and synthesis of mono and few-layers transition metal dichalcogenides by vapour techniques: a review *RSC Adv.* **5** 75500–18

[7] Jo S, Ubrig N, Berger H, Kuzmenko A B and Morpurgo A F 2014 Mono- and bilayer WS_2 light-emitting transistors *Nano Lett.* **14** 2019–25

[8] Gandi A N and Schwingenschlögl U 2014 WS_2 As an excellent high-temperature thermoelectric material *Chem. Mater.* **26** 6628–37

[9] Ovchinnikov D, Allain A, Huang Y S, Dumcenco D and Kis A 2014 Electrical transport properties of single-layer WS_2 *ACS Nano* **8** 8174–81

[10] Chhowalla M, Shin H S, Eda G, Li L J, Loh K P and Zhang H 2013 The chemistry of two-dimensional layered transition metal dichalcogenide nanosheets *Nat. Chem.* **5** 263–75

[11] Schutte W J, Deboer J L and Jellinek F 1987 Crystal-structures of tungsten disulfide and diselenide *J. Solid State Chem.* **70** 207–9

[12] Seifert G, Kohler T and Tenne R 2002 Stability of metal chalcogenide nanotubes *J. Phys. Chem.* B **106** 2497–501

[13] Whitby R L D, Hsu W K, Boothroyd C B, Fearon P K, Kroto H W and Walton D R 2001 Tungsten disulphide sheathed carbon nanotubes *ChemPhysChem* **2** 620–3

[14] Brüser V *et al* 2014 Single- to triple-wall WS_2 nanotubes obtained by high-power plasma ablation of WS_2 multiwall nanotubes *Inorganics* **2** 177–90

[15] Zak A, Sallacan-Ecker L, Margolin A, Genut M and Tenne R 2009 Insight into the growth mechanism of WS_2 nanotubes in the scaled-up fluidized-bed reactor *Nano* **4** 91–8

[16] Li H *et al* 2013 Mechanical exfoliation and characterization of single- and few-layer nanosheets of WSe_2, TaS_2, and $TaSe_2$ *Small* **9** 1974–81

[17] Benameur M M, Radisavljevic B, Heron J S, Sahoo S, Berger H and Kis A 2011 Visibility of dichalcogenide nanolayers *Nanotechnology* **22** 125706

[18] Kang K N, Godin K and Yang E H 2015 The growth scale and kinetics of WS_2 monolayers under varying H_2 concentration *Sci. Rep.* **5** 13205

[19] Smith R J *et al* 2011 Large-scale exfoliation of inorganic layered compounds in aqueous surfactant solutions *Adv. Mater.* **23** 3944–8

[20] Varoon K *et al* 2011 Dispersible exfoliated zeolite nanosheets and their application as a selective membrane *Science* **334** 72–5

[21] Dines M B 1975 Lithium intercalation via N-butyllithium of layered transition-metal dichalcogenides *Mater. Res. Bull.* **10** 287–91

[22] Joensen P, Frindt R F and Morrison S R 1986 Single-layer MoS_2 *Mater. Res. Bull.* **21** 457–61

[23] Splendiani A *et al* 2010 Emerging photoluminescence in monolayer MoS_2 *Nano Lett.* **10** 1271–5

[24] Ding Y, Wang Y, Ni J, Shi L, Shi S and Tang W 2011 First principles study of structural, vibrational and electronic properties of graphene-like MX_2 (M = Mo, Nb, W, Ta; X = S, Se, Te) monolayers *Physica* B **406** 2254–60

[25] Kuc A, Zibouche N and Heine T 2011 Influence of quantum confinement on the electronic structure of the transition metal sulfideTS_2 *Phys. Rev.* B **83** 245213

[26] Ridley B K 1982 The electron-phonon interaction in quasi-two-dimensional semiconductor quantum-well structures *J. Phys. C: Solid State Phys.* **15** 5899–917

[27] Ando T, Fowler A B and Stern F 1982 Electronic properties of two-dimensional systems *Rev. Mod. Phys.* **54** 437–672

[28] Chen J H, Jang C, Xiao S, Ishigami M and Fuhrer M S 2008 Intrinsic and extrinsic performance limits of graphene devices on SiO_2 *Nat. Nanotechnol.* **3** 206–9

[29] Adam S, Hwang E H and Das Sarma S 2008 Scattering mechanisms and Boltzmann transport in graphene *Physica* E **40** 1022–5

[30] Cong C *et al* 2014 Synthesis and optical properties of large-area single-crystalline 2D semiconductor WS_2 monolayer from chemical vapor deposition *Adv. Opt. Mater.* **2** 131–6

[31] Zeng H *et al* 2013 Optical signature of symmetry variations and spin-valley coupling in atomically thin tungsten dichalcogenides *Sci. Rep.* **3** 1608

[32] Verble J L and Wieting T J 1970 Lattice mode degeneracy in MoS_2 and other layer compounds *Phys. Rev. Lett.* **25** 362–5

[33] Sekine T, Nakashizu T, Toyoda K, Uchinokura K and Matsuura E 1980 Raman scattering in layered compound 2H-WS_2 *Solid State Commun.* **35** 371–3

[34] Zhang X, Qiao X F, Shi W, Wu J B, Jiang D S and Tan P H 2015 Phonon and Raman scattering of two-dimensional transition metal dichalcogenides from monolayer, multilayer to bulk material *Chem. Soc. Rev.* **44** 2757–85

[35] Molina-Sánchez A and Wirtz L 2011 Phonons in single-layer and few-layer MoS_2 and WS_2 *Phys. Rev.* B **84** 155413

[36] Mitioglu A A, Plochocka P, Deligeorgis G, Anghel S, Kulyuk L and Maude D K 2014 Second-order resonant Raman scattering in single-layer tungsten disulfideWS_2 *Phys. Rev.* B **89** 245442

[37] Ribeiro-Soares J *et al* 2014 Group theory analysis of phonons in two-dimensional transition metal dichalcogenides *Phys. Rev.* B **90** 115438

[38] Berkdemir A *et al* 2013 Identification of individual and few layers of WS_2 using Raman spectroscopy *Sci. Rep.* **3** 1755

[39] Viršek M, Jesih A, Milošević I, Damnjanović M and Remškar M 2007 Raman scattering of the MoS_2 and WS_2 single nanotubes *Surf. Sci.* **601** 2868–72

[40] Staiger M *et al* 2012 Excitonic resonances in WS_2 nanotubes *Phys. Rev.* B **86** 165423

[41] Zhao W *et al* 2013 Lattice dynamics in mono- and few-layer sheets of WS_2 and WSe_2 *Nanoscale* **5** 9677–83

[42] Lee C, Yan H, Brus L E, Heinz T F, Hone J and Ryu S 2010 Anomalous lattice vibrations of single- and few-layer MoS_2 *ACS Nano* **4** 2695–700

[43] Nayak A P *et al* 2014 Pressure-induced semiconducting to metallic transition in multilayered molybdenum disulphide *Nat. Commun.* **5** 3731

[44] Nayak A P *et al* 2015 Pressure-modulated conductivity, carrier density, and mobility of multilayered tungsten disulfide *ACS Nano* **9** 9117–23

[45] Wang Y, Cong C, Qiu C and Yu T 2013 Raman spectroscopy study of lattice vibration and crystallographic orientation of monolayer MoS_2 under uniaxial strain *Small* **9** 2857–61

[46] Rice C *et al* 2013 Raman-scattering measurements and first-principles calculations of strain-induced phonon shifts in monolayer MoS_2 *Phys. Rev.* B **87** 081307

[47] Zhu C R *et al* 2013 Strain tuning of optical emission energy and polarization in monolayer and bilayer MoS_2 *Phys. Rev.* B **88** 121301

[48] O'Neal K R, Cherian J G, Zak A, Tenne R, Liu Z and Musfeldt J L 2016 High pressure vibrational properties of WS_2 nanotubes *Nano Lett.* **16** 993–9

[49] Ghorbani-Asl M, Zibouche N, Wahiduzzaman M, Oliveira A F, Kuc A and Heine T 2013 Electromechanics in MoS_2 and WS_2: nanotubes versus monolayers *Sci. Rep.* **3** 2961

[50] Yu M 2000 Strength and breaking mechanism of multiwalled carbon nanotubes under tensile load *Science* **287** 637–40

[51] Kaplan-Ashiri I and Tenne R 2007 Mechanical properties of WS_2 nanotubes *J. Cluster Sci.* **18** 549–63

[52] Kaplan-Ashiri I *et al* 2006 On the mechanical behavior of WS_2 nanotubes under axial tension and compression *Proc. Natl Acad. Sci. USA* **103** 523–8

[53] Selvi E, Ma Y, Aksoy R, Ertas A and White A 2006 High pressure x-ray diffraction study of tungsten disulfide *J. Phys. Chem. Solids* **67** 2183–6

[54] Liu K *et al* 2014 Elastic properties of chemical-vapor-deposited monolayer MoS_2, WS_2, and their bilayer heterostructures *Nano Lett.* **14** 5097–103

[55] Bertolazzi S, Brivio J and Kis A 2011 Stretching and breaking of ultrathin MoS_2 *ACS Nano* **5** 9703–9

[56] Zak A *et al* 2011 Scaling up of the WS_2 nanotubes synthesis *Fullerenes, Nanotubes Carbon Nanostruct.* **19** 18–26

[57] Zeng F, Zhang W-B and Tang B-Y 2015 Electronic structures and elastic properties of monolayer and bilayer transition metal dichalcogenides *MX*2 (*M* = Mo, W; *X* = O, S, Se, Te): a comparative first-principles study *Chin. Phys.* B **24** 097103

[58] Giannozzi P, De Gironcoli S, Pavone P and Baroni S 1991 *Ab initio* calculation of phonon dispersions in semiconductors *Phys. Rev.* B **43** 7231–42

[59] Giannozzi P *et al* 2009 QUANTUM ESPRESSO: a modular and open-source software project for quantum simulations of materials *J. Phys.: Condens. Matter* **21** 395502

[60] Vanderbilt D 1990 Soft self-consistent pseudopotentials in a generalized eigenvalue formalism *Phys. Rev.* B **41** 7892–5

[61] Perdew J P and Zunger A 1981 Self-interaction correction to density-functional approximations for many-electron systems *Phys. Rev.* B **23** 5048–79

[62] Zeng F, Zhang W B and Tang B Y 2015 Electronic structures and elastic properties of monolayer and bilayer transition metal dichalcogenides MX2 (M = Mo, W; X = O, S, Se, Te): a comparative first-principles study *Chin. Phys.* B **24** 097103

[63] Monkhorst H J and Pack J D 1976 Special points for Brillouin-zone integrations *Phys. Rev.* B **13** 5188–92

[64] Thomsen C, Reich S and Ordejon P 2002 *Ab initio* determination of the phonon deformation potentials of graphene *Phys. Rev.* B **65** 073403

[65] Li H, Wu J M T, Yin Z Y and Zhang H 2014 Preparation and applications of mechanically exfoliated single-layer and multi-layer MoS_2 and WSe_2 nanosheets *Acc. Chem. Res.* **47** 1067–75

[66] Zhao W J *et al* 2013 Evolution of electronic structure in atomically thin sheets of WS_2 and WSe_2 *ACS Nano* **7** 791–7

[67] Mitioglu A A *et al* 2013 Optical manipulation of the exciton charge state in single-layer tungsten disulfide *Phys. Rev.* B **88** 245403

[68] Rothschild A, Sloan J and Tenne R 2000 Growth of WS_2 nanotubes phases *J. Am. Chem. Soc.* **122** 5169–79

[69] Song J G *et al* 2013 Layer-controlled, wafer-scale, and conformal synthesis of tungsten disulfide nanosheets using atomic layer deposition *ACS Nano* **7** 11333–40

[70] Hajiyev P, Cong C X, Qiu C Y and Yu T 2013 Contrast and Raman spectroscopy study of single- and few-layered charge density wave material: 2H-$TaSe_2$ *Sci. Rep.* **3** 2593

[71] Young R J, Gong L, Kinloch I A, Riaz I, Jalil R and Novoselov K S 2011 Strain mapping in a graphene monolayer nanocomposite *ACS Nano* **5** 3079–84

[72] Gong L *et al* 2013 Reversible loss of bernal stacking during the deformation of few-layer graphene in nanocomposites *ACS Nano* **7** 7287–94

[73] Mohiuddin T M G *et al* 2009 Uniaxial strain in graphene by Raman spectroscopy: G peak splitting, Gruneisen parameters, and sample orientation *Phys. Rev.* B **79** 205433

[74] Gong L, Young R J, Kinloch I A, Riaz I, Jalil R and Novoselov K S 2012 Optimizing the reinforcement of polymer-based nanocomposites by graphene *ACS Nano* **6** 2086–95

[75] Bandaru N *et al* 2014 Effect of pressure and temperature on structural stability of MoS_2 *J. Phys. Chem.* C **118** 3230–5

[76] Conley H J, Wang B, Ziegler J I, Haglund R F, Pantelides S T and Bolotin K I 2013 Bandgap engineering of strained monolayer and bilayer MoS_2 *Nano Lett.* **13** 3626–30